electronics

MDPI

Communication

A Novel Mathematical Approach for Inductor-Current Expressions Definition in Multilevel Dual-Active-Bridge Converters

Eudald Borrell-Pons, Oriol Esquius-Mas, Alber Filba-Martinez * and Lluís Trilla

Institut de Recerca en Energia de Catalunya, 08930 Barcelona, Spain; eborrell@irec-edu.cat (E.B.-P.); oesquius@irec.cat (O.E.-M.); lltrilla@irec.cat (L.T.)
* Correspondence: afilba@irec.cat

Abstract: The study of multilevel dual-active-bridge (DAB) converters has garnered significant attention in recent years thanks to their advantages with respect to the conventional two-level (2L) DAB; namely, its greater performance and its capability to operate at higher voltage. The analysis of the converter high-frequency inductor current (i_L) is crucial, for instance, to compute its root mean square (RMS) value, required to estimate the conduction losses in the converter. The mathematical expression of i_L is piecewise and multiple variations, i.e., modes, exist depending on the modulation parameter values. This increases the complexity of converter performance analytical study. Thus, a more practical and generalizable expression of i_L current is desirable. This paper proposes novel compact analytic expressions for the instantaneous and RMS inductor current in the 2L-*N*L DAB converter, leveraging binary functions to define the piecewise intervals and to identify the mode as a function of the modulation parameter values. The proposed method paves the way for more simple and computationally efficient DAB performance optimization software tools that allow exploring any given converter structures and modulation strategies.

Keywords: dual-active-bridge converter; multilevel converter; RMS value; piecewise analysis; Fourier decomposition; compact analytic expression

check for updates

Citation: Borrell-Pons, E.; Esquius-Mas, O.; Filba-Martinez, A.; Trilla, L. A Novel Mathematical Approach for Inductor-Current Expressions Definition in Multilevel Dual-Active-Bridge Converters. *Electronics* **2024**, *13*, 4476. https://doi.org/10.3390/electronics13224476

Academic Editors: Fernando Bento, Khaled Laadjal and Antonio J. Marques Cardoso

Received: 15 October 2024
Revised: 6 November 2024
Accepted: 9 November 2024
Published: 14 November 2024

Copyright: © 2024 by the authors. Licensee MDPI, Basel, Switzerland. This article is an open access article distributed under the terms and conditions of the Creative Commons Attribution (CC BY) license (https://creativecommons.org/licenses/by/4.0/).

1. Introduction

Dual-active-bridge (DAB) dc-dc converters have become popular in industrial applications due to their great efficiency and power density. As the demand for high-performance power conversion continues to rise, DAB converter topologies have emerged as an attractive solution, particularly in systems that require both bidirectional power flow and galvanic isolation [1,2]. Moreover, the introduction of multilevel (ML) converter-leg topologies in the DAB offer several performance gains [3,4]. For instance, for the same semiconductor device voltage rating, ML topologies allow increasing the dc-port voltages and the converter power rating, compared to conventional two-level (2L) topologies. On the other hand, for the same dc-port voltage, they allow reducing the converter conduction and switching losses by using lower-voltage-rated semiconductor devices with better performance figures and cost benefit ratios. Additionally, ML topologies open the door to advanced modulation techniques that leverage the additional degree of freedom offered by the ML ac-voltage waveforms to further improve the converter performance [5–7]. ML DAB converters have a wide range of applications, such as solid-state transformers [8,9], high-power battery storage systems [10,11], electric vehicles fast-charging stations [12,13] or low-voltage dc distribution systems [14–17]. They may also be applicable to lower power applications, given their comparable better performance as a trade-off of cost and complexity.

The performance analysis of ML DAB converters requires an accurate study of the current flowing through its high-frequency inductor (i_L). For instance, it allows determining the root mean square (RMS) current flowing through the power semiconductor devices and passive components and thus computing their conduction losses. Therefore, an accurate

expression for i_L in the form of a piecewise expression is necessary for the analysis of the converter [7,14,18,19].

However, the piecewise-defined nature of i_L presents a challenge for its study. When any of the DAB ac-voltage waveforms presents more than two voltage levels, different piecewise expressions for i_L arise (known as "modes" or "cases" in the literature), each one valid for different intervals of the modulation parameters, i.e., the phase shift and voltage waveform duty cycles. The number of i_L expressions increases as the number of levels in the ac-voltage waveform increases, for instance, when ML converter leg topologies are employed in the DAB. Thus, ML DAB performance analysis through the analytical study of the i_L piecewise expressions becomes complex and laborious.

To address this challenge, this paper proposes a generalized and compact mathematical function that provides the DAB i_L piecewise expression, employing binary indicator functions to define the piecewise intervals and to identify the mode as a function of the modulation parameter values. The proposed expression is valid for any DAB featuring a two-level square-wave ac voltage on one side and a staircase-wave ac voltage with any number of levels on the other side, i.e., a 2L-NL ML DAB converter. With the proposed generalized function, the paper also provides the generalized function for the DAB inductor RMS current.

The rest of the paper is organized as follows: First, Section 2 derives the proposed generalized function that provides the compact expressions for i_L instantaneous and RMS values for a 2L-NL DAB converter. The generalization to N levels is accomplished by following an inductive process, first analyzing the 2L-3L DAB and 2L-4L DAB cases and finally inferring the generalized function. Then, Section 3 validates the proposed function by comparing numerically and graphically i_L for multiple modulation parameter values against the results obtained through Fourier analysis of the current. Section 4 performs a comparison of the computational time required to obtain i_L instantaneous and RMS values using the compact expressions and through Fourier analysis. Finally, Section 5 discusses the implications of the proposed method and outlines future research work.

2. Derivation of the Generalized Inductor Current Expression

Let us consider the ideal lossless ML DAB converter shown in Figure 1, featuring two 2L converter legs in side a and two NL NPC converter legs in side b, that is, a single-phase 2L-NL DAB converter. Such a converter is capable of synthesizing an ac-voltage waveform with two voltage levels in side a (v_a) and $2N-1$ voltage levels in side b (v_b), as shown in Figure 2a and 2b, respectively. Parameters V_a and V_b are the dc-link voltages of sides a and b of the converter, respectively. Let us consider that the capacitance in the converter dc port is large enough such that v_a and v_b are constant over each waveform step interval. Let us also consider a modulation where v_a and v_b present quarter-wave symmetry and that it works in steady-state operation. As shown in Figure 2, a total of N modulation angles are used, which are defined as the phase shift between v_a and v_b, φ, and the angles controlling the dwell times of the voltage pulses in v_b, $\{\alpha_1, \alpha_2, ..., \alpha_M\}$, where $M = N-1$ and

$$0 \leq \varphi \leq \frac{\pi}{2} \tag{1}$$

$$0 \leq \alpha_1 \leq ... \leq \alpha_M \leq \pi. \tag{2}$$

It should be noted that other ML converter-leg topologies could be considered, such as flying-capacitor [20] or modular-ML [21] topologies.

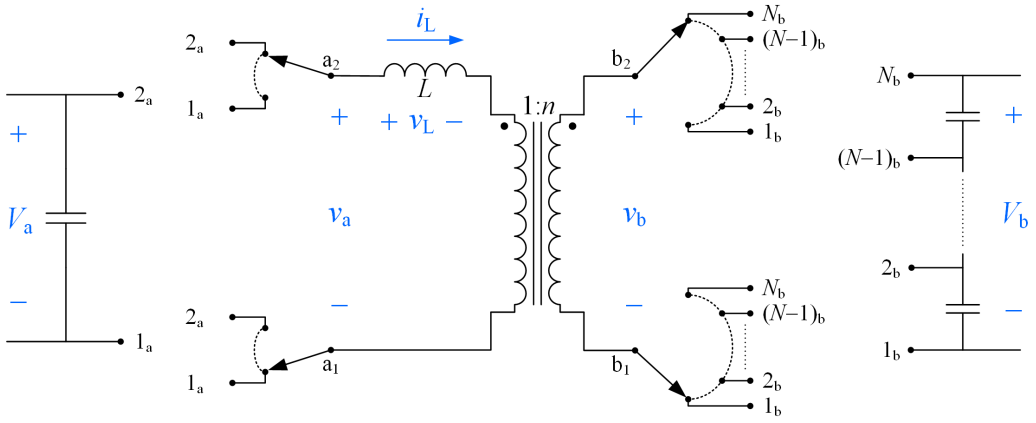
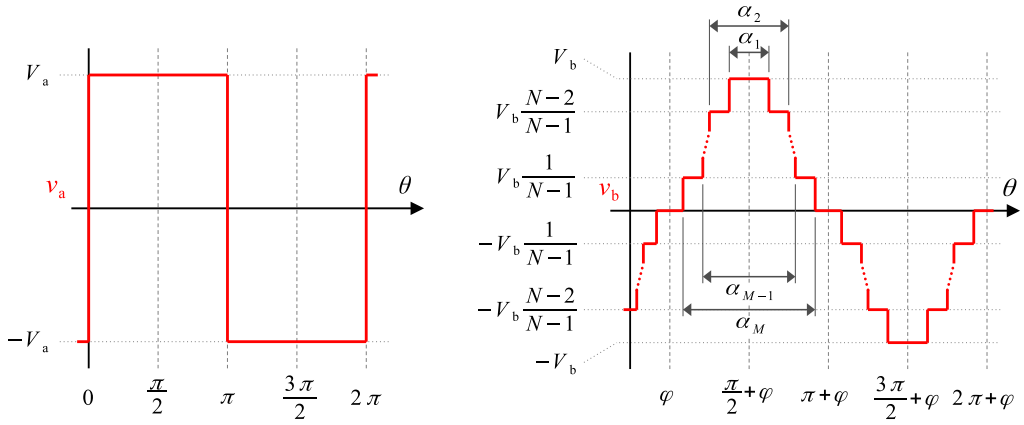


Figure 1. Topology of the considered ML DAB converter. Neutral-point-clamped (NPC) converter legs are considered, represented as single-pole double-throw switches in side a and as single-pole multiple-throw switches in side b. Relevant electrical variables are shown in blue.



(a) **(b)**

Figure 2. Synthesized ac-voltage waveforms and modulation parameters in the considered 2L-*N*L DAB. (**a**) a-side voltage (v_a). (**b**) b-side voltage (v_b) and its modulation parameters.

2.1. 2L-3L DAB Instantaneous Current Compact Expression

The voltage across the series inductor in the DAB converter, v_L, is

$$v_L = v_a - \frac{v_b}{n}, \tag{3}$$

where n is the inverse of the converter transformer turns ratio. Then, the slope of the current through the inductor, i_L, is

$$\frac{di_L}{dt} = \frac{v_a - v_b/n}{L}, \tag{4}$$

where L is the equivalent inductance given by the series connection of the transformer leakage inductance and an external series inductor. Given the stepped nature of voltages v_a and v_b, the mathematical expression of i_L is piecewise-defined, where each segment of the piecewise current shape is delimited by the instants when v_a and v_b feature a rising or falling edge (switching instants). Figure 3 shows three examples of v_a, v_b, and i_L. This figure reveals that, for a given V_a, V_b, n, and L, the sequence of slope values present in i_L within a switching period ($\theta \in [0, 2\pi]$) depends on the specific values of the modulation parameters. For instance, in the i_L waveform shown in Figure 3a, the first interval ($\left[0, \frac{\pi}{2} - \frac{\alpha_2}{2}\right]$) has

a slope $\frac{di_L}{dt} = \frac{V_a}{L}$, the second interval ($\left[\frac{\pi}{2} - \frac{\alpha_2}{2}, \frac{\pi}{2} - \frac{\alpha_1}{2}\right]$) has $\frac{di_L}{dt} = \frac{V_a - V_b/(2n)}{L}$ and so on. However, in Figure 3b, the first interval ($\left[0, \varphi - \frac{\pi}{2} + \frac{\alpha_2}{2}\right]$) has a slope $\frac{di_L}{dt} = \frac{V_a + V_b/(2n)}{L}$, the second interval ($\left[\varphi - \frac{\pi}{2} + \frac{\alpha_2}{2}, \varphi + \frac{\pi}{2} - \frac{\alpha_2}{2}\right]$) has a slope $\frac{di_L}{dt} = \frac{V_a}{L}$, and so on. From Figure 3, it can be inferred that different piecewise expressions for i_L exist depending on the position of the v_b switching instants with respect to those of v_a; i.e., different modes exist.

In the 2L-3L DAB three different modes arise, referred to as Mode 0, Mode 1, and Mode 2 (c.f. Figure 3). One can identify each mode with

$$\begin{cases} \frac{3\pi}{2} + \frac{\alpha_1}{2} + \varphi < 2\pi \begin{cases} \frac{3\pi}{2} + \frac{\alpha_2}{2} + \varphi < 2\pi & \text{Mode 0} \\ \frac{3\pi}{2} + \frac{\alpha_2}{2} + \varphi \geq 2\pi & \text{Mode 1} \end{cases} \\ \frac{3\pi}{2} + \frac{\alpha_1}{2} + \varphi \geq 2\pi \quad \text{Mode 2} \end{cases} . \tag{5}$$

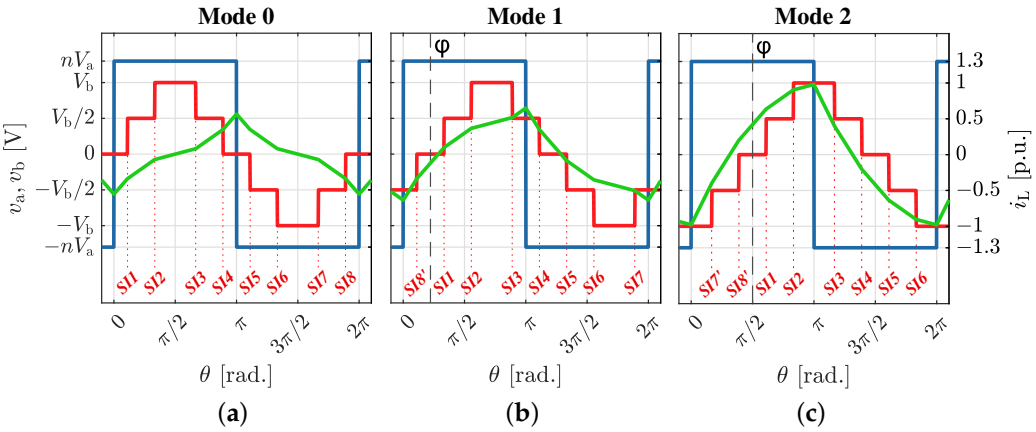


Figure 3. ac-voltages v_a (blue waveform) and v_b (red) and current i_L (green) for different modes in the 2L-3L DAB converter. All current values are divided by the peak current in Mode 2. Switching angles are $\{\alpha_1, \alpha_2\} = \{\frac{\pi}{3}, \frac{7\pi}{9}\}$ (**a**) Mode 0, with $\varphi = 0$. (**b**) Mode 1, with $\varphi = \frac{2\pi}{9}$. (**c**) Mode 2, with $\varphi = \frac{\pi}{2}$.

Based on Equation (5), let us define the binary function K_j associated to $\alpha_j, j \in \{1, 2\}$ as

$$K_j(\varphi, \alpha_j) = \left\lfloor \frac{\frac{3\pi}{2} + \frac{\alpha_j}{2} + \varphi}{2\pi} \right\rfloor, \tag{6}$$

to allow for an automatic detection of each mode for a given set of modulation parameter values. The values of K_1 and K_2 for each mode in the 2L-3L converter are

$$\text{Mode 0} \begin{cases} K_1 = 0 \\ K_2 = 0 \end{cases} \quad \text{Mode 1} \begin{cases} K_1 = 0 \\ K_2 = 1 \end{cases} \quad \text{Mode 2} \begin{cases} K_1 = 1 \\ K_2 = 1 \end{cases} . \tag{7}$$

Let us now define v_a and v_b over the whole switching period by means of the indicator function $\mathbb{1}(\theta)_{[\theta_0, \theta_1]}$ and the binary function $K_j(\varphi, \alpha_j)$ defined previously, such that

$$v_a(\theta) = V_a \cdot \mathbb{1}(\theta)_{[0,\pi]} - V_a \cdot \mathbb{1}(\theta)_{[\pi, 2\pi]}, \tag{8}$$

$$\begin{aligned} v_{\mathrm{b}}(\theta;\varphi,\alpha_1,\alpha_2) = {} & \frac{V_{\mathrm{b}}}{2}\cdot\mathbb{1}(\theta)_{[SI1,\,SI2]\cup[SI3,\,SI4]} + V_{\mathrm{b}}\cdot\mathbb{1}(\theta)_{[SI2,\,SI3]} - \frac{V_{\mathrm{b}}}{2}\cdot\mathbb{1}(\theta)_{[SI5,\,SI6]} \\ & + (1-K_2)\left(-V_{\mathrm{b}}\cdot\mathbb{1}(\theta)_{[SI6,\,SI7]} - \frac{V_{\mathrm{b}}}{2}\cdot\mathbb{1}(\theta)_{[SI7,\,SI8]}\right) \\ & + K_2(1-K_1)\left(-V_{\mathrm{b}}\cdot\mathbb{1}(\theta)_{[SI6,\,SI7]} - \frac{V_{\mathrm{b}}}{2}\cdot\mathbb{1}(\theta)_{[SI7,\,2\pi]\cup[0,\,SI8']}\right) \\ & + K_1\left(-V_{\mathrm{b}}\cdot\mathbb{1}(\theta)_{[SI6,\,2\pi]\cup[0,\,SI7']} - \frac{V_{\mathrm{b}}}{2}\cdot\mathbb{1}(\theta)_{[SI7',\,SI8']}\right), \end{aligned} \tag{9}$$

where $\mathbb{1}(\theta)_{[\theta_0,\theta_1]} = 1$ when $\theta \in [\theta_0,\theta_1]$ and $\mathbb{1}(\theta)_{[\theta_0,\theta_1]} = 0$ otherwise, and

$$\begin{cases} SI1 = \dfrac{\pi}{2} - \dfrac{\alpha_2}{2} + \varphi \\ SI2 = \dfrac{\pi}{2} - \dfrac{\alpha_1}{2} + \varphi \\ SI3 = \dfrac{\pi}{2} + \dfrac{\alpha_1}{2} + \varphi \\ SI4 = \dfrac{\pi}{2} + \dfrac{\alpha_2}{2} + \varphi \\ SI5 = \dfrac{3\pi}{2} - \dfrac{\alpha_2}{2} + \varphi \\ SI6 = \dfrac{3\pi}{2} - \dfrac{\alpha_1}{2} + \varphi \\ SI7 = \dfrac{3\pi}{2} + \dfrac{\alpha_1}{2} + \varphi \\ SI8 = \dfrac{3\pi}{2} + \dfrac{\alpha_2}{2} + \varphi \\ SI7' = SI7 - 2\pi \\ SI8' = SI8 - 2\pi \end{cases} \tag{10}$$

correspond to the switching instants of v_{b} as depicted in Figure 3.

The instantaneous current through the series inductance is

$$i_{\mathrm{L}}(\theta;\varphi,\alpha_1,\alpha_2) = \frac{1}{2\pi f L}\int_0^{\theta}\left(v_{\mathrm{a}}(x) - \frac{v_{\mathrm{b}}(x;\varphi,\alpha_1,\alpha_2)}{n}\right)\cdot dx + i_{\mathrm{L}}(0), \tag{11}$$

where f is the converter switching frequency. Let us separate the integral terms in Equation (11) into two terms, such as

$$i_{\mathrm{L}}(\theta) = \frac{1}{2\pi f L}\left(\int_0^{\theta} v_{\mathrm{a}}(x)\cdot dx - \int_0^{\theta}\frac{v_{\mathrm{b}}(x)}{n}\cdot dx\right) + i_{\mathrm{L}}(0). \tag{12}$$

Let us also define the integral of an indicator function using the min function, such as

$$\int_0^{\theta}\mathbb{1}(x)_{[\theta_0,\theta_1]}dx = \min\{\theta,\theta_1\} - \min\{\theta,\theta_0\} \quad \forall\,\theta,\theta_0,\theta_1 \in [0,2\pi]. \tag{13}$$

The expressions of v_{a} and v_{b} can now be substituted into Equation (12) to obtain the compact i_{L} expression. On the one hand, the $\int_0^{\theta} v_{\mathrm{a}}(x)\cdot dx$ term in Equation (12) is solved as

$$\begin{aligned} \int_0^{\theta} v_{\mathrm{a}}(x)\cdot dx &= \int_0^{\theta}\left(V_{\mathrm{a}}\cdot\mathbb{1}(x)_{[0,\pi]} - V_{\mathrm{a}}\cdot\mathbb{1}(x)_{[\pi,2\pi]}\right)dx \\ &= -V_{\mathrm{a}}\theta + 2V_{\mathrm{a}}\min\{\theta,\pi\}. \end{aligned} \tag{14}$$

On the other hand, solving $\int_0^\theta \frac{v_b(x)}{n} \cdot dx$ involves integrating both $\mathbb{1}(x)_{[\theta_0,\theta_1]}$ and K_j functions. Since the value of K_j does not depend on the variable of integration (θ), it is treated as a constant parameter, facilitating the resolution of the integral. The result is simplified by grouping the common factors of the expression, and

$$\int_0^\theta \frac{v_b(x)}{n} \cdot dx = \frac{\gamma_2}{n} V_b \cdot \theta + \frac{V_b}{4\pi n f L}(A_1 - B_1 + A_2 - B_2), \tag{15}$$

solution is obtained, where γ_2, A_j and B_j are defined as

$$\gamma_2(\varphi, \alpha_1, \alpha_2) = \frac{K_1 + K_2}{2}, \tag{16}$$

$$\begin{aligned} A_j(\theta; \varphi, \alpha_j) &= \min\left\{\theta, \frac{\pi}{2} - \frac{\alpha_j}{2} + \varphi\right\} - \min\left\{\theta, \frac{\pi}{2} + \frac{\alpha_j}{2} + \varphi\right\} \\ B_j(\theta; \varphi, \alpha_j) &= \min\left\{\theta, \frac{3\pi}{2} - \frac{\alpha_j}{2} + \varphi\right\} - \min\left\{\theta, \frac{3\pi}{2} + \frac{\alpha_j}{2} + \varphi - 2\pi K_j\right\} \end{aligned}. \tag{17}$$

Then, from Equations (12), (14), and (15),

$$\begin{aligned} i_L(\theta) = &\frac{1}{2\pi f L}\left[\left(\frac{\gamma_2}{n} V_b - V_a\right)\theta + 2V_a \min\{\theta, \pi\}\right] \\ &+ \frac{V_b}{4\pi n f L}(A_1 - B_1 + A_2 - B_2) + i_L(0) \end{aligned} \tag{18}$$

is obtained.

In the DAB converter, the average value for the inductor current over a switching period is zero, i.e., $\int_0^{2\pi} i_L(\theta) \cdot d\theta = 0$. Then,

$$i_L(0) = -\frac{1}{2\pi} \int_0^{2\pi} (i_L(\theta) - i_L(0)) \cdot d\theta. \tag{19}$$

Solving $i_L(0)$ in Equation (19) and substituting it into Equation (18), the compact analytic expression for i_L in a 2L-3L DAB converter is obtained, such as

$$\begin{aligned} i_L(\theta; \varphi, \alpha_1, \alpha_2) = &\frac{1}{2\pi f L}\left[\frac{\gamma_2}{n} V_b(\theta - \pi) - V_a\left(\frac{\pi}{2} + \theta\right) + 2V_a \min\{\theta, \pi\}\right] \\ &+ \frac{V_b}{8\pi n f L}[2A_1 - 2B_1 + \alpha_1 + K_1(3\pi - \alpha_1 - 2\varphi)] \\ &+ \frac{V_b}{8\pi n f L}[2A_2 - 2B_2 + \alpha_2 + K_2(3\pi - \alpha_2 - 2\varphi)]. \end{aligned} \tag{20}$$

Note that Equation (20) transitions smoothly between consecutive modes; i.e., the expression for i_L is the same when the boundary condition is met. For example, the boundary between Mode 0 to Mode 1 is defined by $\frac{3\pi}{2} + \frac{\alpha_M}{2} + \varphi = 2\pi$. Imposing this condition to Equation (20) on Mode 0 and on Mode 1 results in the same mathematical expression.

2.2. Generalized Current Compact Expression of a 2L-NL DAB

Defining the compact analytical expression for the instantaneous current through the series inductor in a 2L-3L DAB enables us to generalize $i_L(\theta)$ for a 2L-NL DAB using an inductive process.

First, the compact analytical expression for $i_{\mathrm{L}}(\theta)$ in a 2L-4L DAB is derived following the methodology employed for the 2L-3L converter, such as

$$\begin{aligned} i_{\mathrm{L}}(\theta;\varphi,\alpha_1,\alpha_2,\alpha_3) = {} & \frac{1}{2\pi fL}\left[\frac{\gamma_3}{n}V_{\mathrm{b}}(\theta-\pi) - V_{\mathrm{a}}\left(\frac{\pi}{2}+\theta\right) + 2V_{\mathrm{a}}\min\{\theta,\pi\}\right] \\ & + \frac{V_{\mathrm{b}}}{12\pi nfL}[2A_1 - 2B_1 + \alpha_1 + K_1(3\pi - \alpha_1 - 2\varphi)] \\ & + \frac{V_{\mathrm{b}}}{12\pi nfL}[2A_2 - 2B_2 + \alpha_2 + K_2(3\pi - \alpha_2 - 2\varphi)] \\ & + \frac{V_{\mathrm{b}}}{12\pi nfL}[2A_3 - 2B_3 + \alpha_3 + K_3(3\pi - \alpha_3 - 2\varphi)] \end{aligned}, \tag{21}$$

where γ_3 is defined as

$$\gamma_3(\varphi,\alpha_1,\alpha_2,\alpha_3) = \frac{K_1+K_2+K_3}{3}. \tag{22}$$

Equations (20) and (21) let us define the structure of the expression for $i_{\mathrm{L}}(\theta;\varphi,\alpha_1,\ldots,\alpha_M)$, with the number of levels at side b of the converter, N, and the number of modulation angles controlling the amplitude of the pulses of v_{b}, M, treated as parameters. Then, the generalized compact expression for $i_{\mathrm{L}}(\theta;\varphi,\alpha_1,\ldots,\alpha_M)$ in a 2L-NL DAB is defined as

$$\begin{aligned} i_{\mathrm{L}}(\theta;\varphi,\alpha_1,\ldots,\alpha_M) = {} & \frac{1}{2\pi fL}\left[\frac{\gamma_M}{n}V_{\mathrm{b}}(\theta-\pi) - V_{\mathrm{a}}\left(\frac{\pi}{2}+\theta\right) + 2V_{\mathrm{a}}\min\{\theta,\pi\}\right] \\ & + \frac{V_{\mathrm{b}}}{4\pi nMfL}\sum_{j=1}^{M}\left[2A_j - 2B_j + \alpha_j + K_j(3\pi - \alpha_j - 2\varphi)\right], \end{aligned} \tag{23}$$

where γ_M is

$$\gamma_M(\varphi,\alpha_1,\ldots,\alpha_M) = \frac{\sum_{j=1}^{M}K_j}{M}. \tag{24}$$

2.3. RMS Expression

The RMS expression for the inductor current in a 2L-NL DAB is defined as

$$I_{\mathrm{L,RMS}} = \sqrt{\frac{1}{2\pi}\int_0^{2\pi} i_{\mathrm{L}}^2(\theta)d\theta}. \tag{25}$$

Then, from Equations (23) and (25), the generalized compact expression for $I_{\mathrm{L,RMS}}$ is obtained using the MATLAB R2023b Symbolic Math Toolbox, resulting in

$$\begin{aligned} I_{\mathrm{L,RMS}} = {} & \frac{1}{(2\pi)^{3/2}fL}\left[\frac{2\pi^3}{3}\frac{\gamma_M^2}{n^2}V_{\mathrm{b}}^2 + \frac{1}{6}\pi^3V_{\mathrm{a}}^2 + 2\frac{V_{\mathrm{b}}^2}{M^2n^2}\sum_{1\le i<j\le M}P_{i,j}\right. \\ & \left. + \frac{1}{M}\sum_{j=1}^{M}\left(\frac{2V_{\mathrm{b}}^2}{n^2}\gamma_M U_j + \frac{2V_{\mathrm{b}}}{n}V_{\mathrm{a}}W_j + \frac{V_{\mathrm{b}}^2}{Mn^2}P_{j,j}\right)\right]^{1/2} \end{aligned} \tag{26}$$

where

$$
\begin{aligned}
U_j &= -\pi\alpha_j\varphi - K_j\Big(\frac{\pi}{12}(5\pi^2 + 6\pi\alpha_j + 12\pi\varphi - 3\alpha_j^2 - 12\alpha_j\varphi - 12\varphi^2)\Big),\\
W_j &= \frac{\alpha_j}{12}(-3\pi^2 + \alpha_j^2 + 12\varphi^2) - K_j\frac{1}{12}(\alpha_j - \pi + 2\varphi)^3,\\
P_{i,j} &= -\frac{\alpha_i}{12}\Big(\alpha_i^2 + 3\alpha_j^2 - 6\pi\alpha_j\Big) + K_j\pi\alpha_i\varphi\\
&\quad + K_i\left(\frac{19\pi^3}{6} - \frac{\pi^2\alpha_i}{2} + \frac{\pi^2\alpha_j}{2} - \frac{\pi\alpha_i^2}{4} - \pi\alpha_i\varphi - \frac{\pi\alpha_j^2}{4} - 2\pi\varphi^2 + \frac{\alpha_i^3}{48} - \frac{\alpha_i^2\alpha_j}{16} + \frac{\alpha_i\alpha_j^2}{16} - \frac{\alpha_j^3}{48}\right)\\
&\quad + K_iK_j\left(-3\pi^3 + \pi^2\alpha_i + 2\varphi\pi^2 - \frac{\alpha_i^3}{48} + \frac{\alpha_i^2\alpha_j}{16} - \frac{\alpha_i\alpha_j^2}{16} + \frac{\alpha_j^3}{48}\right).
\end{aligned}
\tag{27}
$$

3. Numerical Verification

To verify the proposed DAB inductor current compact expression, the results obtained with the proposed approach are compared with reference results; i.e., results obtained through Fourier analysis up to the 2000th harmonic. Then, this section presents the instantaneous and RMS current expressions derived from the Fourier analysis, the numerical verification of the compact analytic expressions for the 2L-3L DAB, and the 2L-4L DAB.

The MATLAB code implementing the functions to compute the inductor-current instantaneous and RMS values with the proposed compact approach are provided as Supplementary Files.

3.1. 2L-NL DAB Instantaneous and RMS Current Expressions Through Fourier Analysis

The expressions for the ac voltage waveforms in a 2L-*N*L DAB (Figure 2) obtained through Fourier analysis are

$$v_{\mathrm{a}} = \sum_h [||\mathbf{V}_{\mathrm{a},h}||\sin(h\theta + \arg(\mathbf{V}_{\mathrm{a},h}))] \tag{28}$$

$$v_{\mathrm{b}} = \sum_h [||\mathbf{V}_{\mathrm{b},h}||\sin(h\theta + \arg(\mathbf{V}_{\mathrm{b},h}))], \tag{29}$$

where h is the harmonic index and $\mathbf{V}_{\mathrm{a},h}$ and $\mathbf{V}_{\mathrm{b},h}$ are the hth-harmonic voltage phasors,

$$
\begin{aligned}
\mathbf{V}_{\mathrm{a},h} &= V_{\mathrm{a},h}\\
\mathbf{V}_{\mathrm{b},h} &= V_{\mathrm{b},h}(\cos(h\varphi) - i\cdot\sin(h\varphi))\\
V_{\mathrm{a},h} &= \frac{2V_{\mathrm{a}}}{\pi h}[1 - \cos(h\pi)]\\
V_{\mathrm{b},h} &= \frac{2V_{\mathrm{b}}}{(N-1)\pi h}\sum_{j=1}^{M}\left[\cos\left(h\left(\frac{\pi}{2} - \frac{\alpha_j}{2}\right)\right) - \cos\left(h\left(\frac{\pi}{2} + \frac{\alpha_j}{2}\right)\right)\right]
\end{aligned}
\quad , \tag{30}
$$

and $V_{\mathrm{a},h}$ and $V_{\mathrm{b},h}$ are the amplitudes of the v_{a} and v_{b} hth harmonic, respectively. Then, from Equations (3) and (4), the hth-harmonic component of the inductor-current phasor is defined as

$$\mathbf{I}_{\mathrm{L},h} = \frac{\mathbf{V}_{\mathrm{a},h} - \mathbf{V}_{\mathrm{b},h}/n}{i\cdot(2\pi h f L)}. \tag{31}$$

Then, the expression for the instantaneous current through the series inductor obtained through Fourier analysis is defined as

$$i_{\mathrm{L}}(\theta) = \sum_h [||\mathbf{I}_{\mathrm{L},h}||\sin(h\theta + \arg(\mathbf{I}_{\mathrm{L},h}))], \tag{32}$$

and its RMS value is obtained from

$$I_{\mathrm{L,RMS}} = \sqrt{\frac{1}{2}\sum_{h} ||\mathbf{I}_{\mathrm{L},h}||^2}. \tag{33}$$

3.2. Numerical Verification for the 2L-3L DAB

Tables 1 and 2 provide a comparison of the i_{L} and $I_{\mathrm{L,RMS}}$ per-unit (p.u.) values for the 2L-3L DAB as obtained from the compact analytical expressions (Equation (23) and Equation (26), respectively) and from the Fourier analysis (Equation (32) and Equation (33), respectively). The Table 1 results are obtained for three distinct operation points, defined by the modulation angles φ, α_1, and α_2, and at five arbitrary values of θ. The values of the modulation angles have been selected such that each operation point corresponds to a specific mode (Mode 0, Mode 1, and Mode 2, defined in Section 2.1). The Table 2 results are obtained for the same modulation angles as Table 1. The instantaneous and RMS current values obtained using the analytical expression and the Fourier approximation are found to be equal at all three operating points. Furthermore, Figure 4 provides a visual comparison of the i_{L} waveform obtained using the analytic expression and the Fourier approximation (same operation points as Table 1). As shown, both waveforms are identical throughout the entire switching cycle.

Table 1. Numerical comparison of $i_{\mathrm{L}}(\theta)$ using the compact analytical expression ($i_{\mathrm{L,Comp}}$) and the Fourier approximation ($i_{\mathrm{L,Fourier}}$). All current values are divided by the peak current in Figure 4c.

	Mode 0: $\{\varphi, \alpha_1, \alpha_2\} = \{\frac{1}{6}\pi, \frac{5}{18}\pi, \frac{7}{18}\pi\}$		**Mode 1:** $\{\varphi, \alpha_1, \alpha_2\} = \{\frac{1}{6}\pi, \frac{5}{18}\pi, \frac{29}{36}\pi\}$		**Mode 2:** $\{\varphi, \alpha_1, \alpha_2\} = \{\frac{1}{3}\pi, \frac{7}{18}\pi, \frac{29}{36}\pi\}$	
θ **[rad]**	$i_{\mathrm{L,Comp}}$ **[p.u.]**	$i_{\mathrm{L,Fourier}}$ **[p.u.]**	$i_{\mathrm{L,Comp}}$ **[p.u.]**	$i_{\mathrm{L,Fourier}}$ **[p.u.]**	$i_{\mathrm{L,Comp}}$ **[p.u.]**	$i_{\mathrm{L,Fourier}}$ **[p.u.]**
0	−1.00	−1.00	−0.79	−0.79	−1	−1
1	−0.05	−0.05	0.19	0.19	0.35	0.35
2	0.50	0.50	0.50	0.50	0.99	0.99
3	0.86	0.86	0.72	0.72	1	1
4	0.18	0.18	−0.12	−0.12	−0.22	−0.22

Table 2. Numerical comparison of $I_{\mathrm{L,RMS}}$ using the compact analytical expression ($i_{\mathrm{L,Comp}}$) and the Fourier approximation ($i_{\mathrm{L,Fourier}}$). All current values are divided by the peak current in Figure 4c.

Mode 0: $\{\varphi, \alpha_1, \alpha_2\} = \{\frac{1}{6}\pi, \frac{5}{18}\pi, \frac{7}{18}\pi\}$		**Mode 1:** $\{\varphi, \alpha_1, \alpha_2\} = \{\frac{1}{6}\pi, \frac{5}{18}\pi, \frac{29}{36}\pi\}$		**Mode 2:** $\{\varphi, \alpha_1, \alpha_2\} = \{\frac{1}{3}\pi, \frac{7}{18}\pi, \frac{29}{36}\pi\}$	
$i_{\mathrm{L,RMS,Comp}}$ **[p.u.]**	$i_{\mathrm{L,RMS,Fourier}}$ **[p.u.]**	$i_{\mathrm{L,RMS,Comp}}$ **[p.u.]**	$i_{\mathrm{L,RMS,Fourier}}$ **[p.u.]**	$i_{\mathrm{L,RMS,Comp}}$ **[p.u.]**	$i_{\mathrm{L,RMS,Fourier}}$ **[p.u.]**
0.55	0.55	0.47	0.47	0.78	0.78

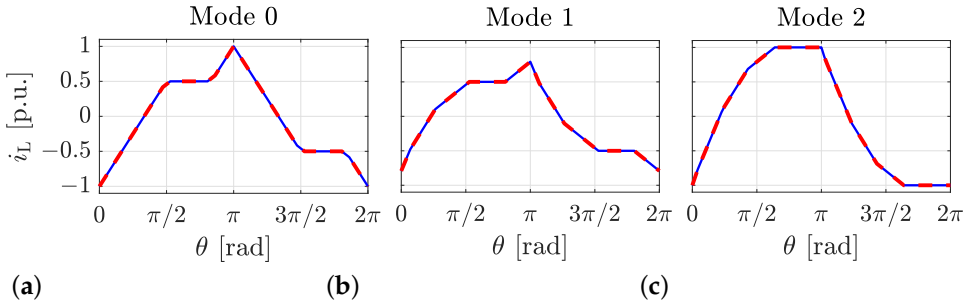


Figure 4. Waveform of $i_L(\theta)$ obtained using the compact analytic expression (solid blue line) and the Fourier approximation (dashed red line) at three different operation points. All current values are divided by the peak current in (**c**). (**a**) Mode 0, with $\{\varphi, \alpha_1, \alpha_2\} = \left\{\frac{1}{6}\pi, \frac{5}{18}\pi, \frac{7}{18}\pi\right\}$. (**b**) Mode 1, with $\{\varphi, \alpha_1, \alpha_2\} = \left\{\frac{1}{6}\pi, \frac{5}{18}\pi, \frac{29}{36}\pi\right\}$. (**c**) Mode 2, with $\{\varphi, \alpha_1, \alpha_2\} = \left\{\frac{1}{3}\pi, \frac{7}{18}\pi, \frac{29}{36}\pi\right\}$.

3.3. Numerical Verification for the 2L-4L DAB

For the purpose of validating the presented compact analytical expressions for the instantaneous and RMS inductor currents, the same verification conducted in Section 3.2 is performed for a 2L-4L DAB. Tables 3 and 4 provide a comparison of the i_L and $I_{L,RMS}$ p.u. values for the 2L-4L DAB as obtained from the compact analytical expressions and from the Fourier analysis.

In a 2L-4L DAB converter, four modes arise. The Tables 3 and 4 results are obtained for four distinct operation points, each operation point corresponding to a specific mode. As can be seen from both tables, the instantaneous and RMS current values obtained using the analytical expression and the Fourier approximation are equal at all four operating points. Furthermore, the visual comparison of the i_L waveform in Figure 5 shows that the analytic expression yields the same results as the Fourier approximation throughout the entire switching cycle for all four operation points (same operation points as Table 3). These results consequently validate the analytical expressions presented in this document.

Table 3. Numerical comparison of $i_L(\theta)$ using the compact analytical expression ($i_{L,Comp}$) and the Fourier approximation ($i_{L,Fourier}$). All current values are divided by the peak current in Figure 5a.

	Mode 0: $\{\varphi, \alpha_1, \alpha_2, \alpha_3\} = \{\frac{1}{6}\pi, \frac{1}{18}\pi, \frac{4}{18}\pi, \frac{7}{18}\pi\}$		**Mode 1:** $\{\varphi, \alpha_1, \alpha_2, \alpha_3\} = \{\frac{1}{6}\pi, \frac{4}{18}\pi, \frac{7}{18}\pi, \frac{29}{36}\pi\}$		**Mode 2:** $\{\varphi, \alpha_1, \alpha_2, \alpha_3\} = \{\frac{1}{3}\pi, \frac{4}{18}\pi, \frac{7}{18}\pi, \frac{29}{36}\pi\}$		**Mode 3:** $\{\varphi, \alpha_1, \alpha_2, \alpha_3\} = \{\frac{1}{3}\pi, \frac{7}{18}\pi, \frac{20}{36}\pi, \frac{30}{36}\pi\}$	
θ **[rad]**	$i_{L,Comp}$ **[p.u.]**	$i_{L,Fourier}$ **[p.u.]**	$i_{L,Comp}$ **[p.u.]**	$i_{L,Fourier}$ **[p.u.]**	$i_{L,Comp}$ **[p.u.]**	$i_{L,Fourier}$ **[p.u.]**	$i_{L,Comp}$ **[p.u.]**	$i_{L,Fourier}$ **[p.u.]**
0	−1	−1	−0.74	−0.74	−0.90	−0.90	−0.86	−0.86
1	−0.18	−0.18	0.09	0.09	0.14	0.14	0.29	0.29
2	0.43	0.43	0.43	0.43	0.78	0.78	0.86	0.86
3	0.88	0.88	0.66	0.66	0.87	0.87	0.86	0.86
4	0.30	0.30	−0.02	−0.02	−0.02	−0.02	−0.18	−0.18

Table 4. Numerical comparison of $I_{L,RMS}$ using the compact analytical expression ($i_{L,Comp}$) and the Fourier approximation ($i_{L,Fourier}$). All current values are divided by the peak current in Figure 5a.

Mode 0: $\{\varphi, \alpha_1, \alpha_2, \alpha_3\} = \{\frac{1}{6}\pi, \frac{1}{18}\pi, \frac{4}{18}\pi, \frac{7}{18}\pi\}$		**Mode 1:** $\{\varphi, \alpha_1, \alpha_2, \alpha_3\} = \{\frac{1}{6}\pi, \frac{4}{18}\pi, \frac{7}{18}\pi, \frac{29}{36}\pi\}$		**Mode 2:** $\{\varphi, \alpha_1, \alpha_2, \alpha_3\} = \{\frac{1}{3}\pi, \frac{4}{18}\pi, \frac{7}{18}\pi, \frac{29}{36}\pi\}$		**Mode 3:** $\{\varphi, \alpha_1, \alpha_2, \alpha_3\} = \{\frac{1}{3}\pi, \frac{7}{18}\pi, \frac{20}{36}\pi, \frac{30}{36}\pi\}$	
$i_{L,RMS,Comp}$ **[p.u.]**	$i_{L,RMS,Fourier}$ **[p.u.]**	$i_{L,RMS,Comp}$ **[p.u.]**	$i_{L,RMS,Fourier}$ **[p.u.]**	$i_{L,RMS,Comp}$ **[p.u.]**	$i_{L,RMS,Fourier}$ **[p.u.]**	$i_{L,RMS,Comp}$ **[p.u.]**	$i_{L,RMS,Fourier}$ **[p.u.]**
0.55	0.55	0.42	0.42	0.65	0.65	0.67	0.67

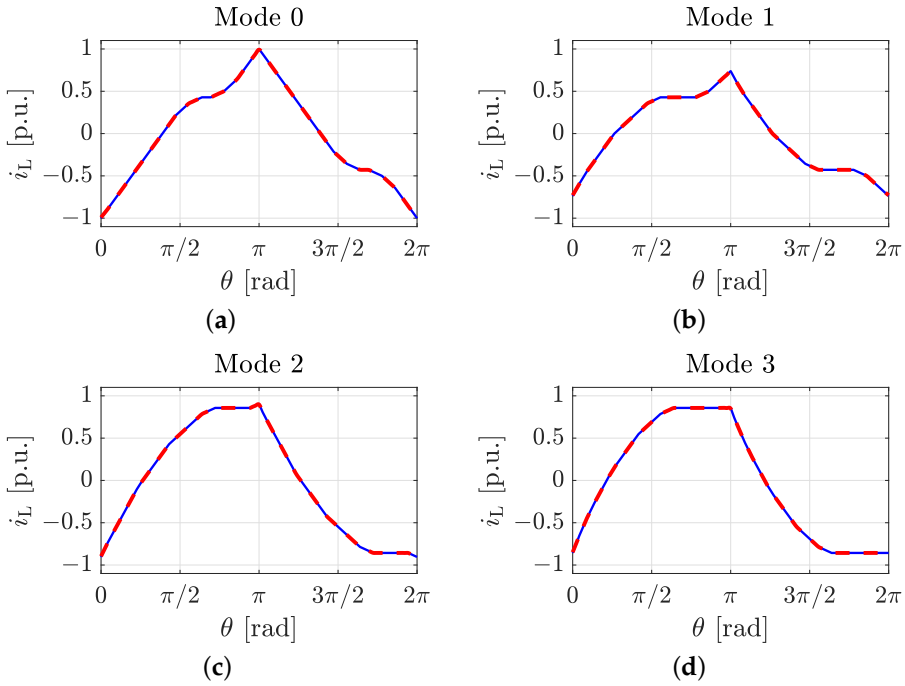


Figure 5. Waveform of $i_L(\theta)$ obtained using the compact analytic expression (solid blue line) and the Fourier approximation (dashed red line) at three different operation points. All current values are divided by the peak current in (**a**). (**a**) Mode 0, with $\{\varphi, \alpha_1, \alpha_2, \alpha_3\} = \left\{\frac{1}{6}\pi, \frac{1}{18}\pi, \frac{4}{18}\pi, \frac{7}{18}\pi\right\}$. (**b**) Mode 1, with $\{\varphi, \alpha_1, \alpha_2, \alpha_3\} = \left\{\frac{1}{6}\pi, \frac{4}{18}\pi, \frac{7}{18}\pi, \frac{29}{36}\pi\right\}$. (**c**) Mode 2, with $\{\varphi, \alpha_1, \alpha_2, \alpha_3\} = \left\{\frac{1}{3}\pi, \frac{4}{18}\pi, \frac{7}{18}\pi, \frac{29}{36}\pi\right\}$. (**d**) Mode 3, with $\{\varphi, \alpha_1, \alpha_2, \alpha_3\} = \left\{\frac{1}{3}\pi, \frac{7}{18}\pi, \frac{20}{36}\pi, \frac{30}{36}\pi\right\}$.

4. Comparative Computational Time Analysis

When developing software tools for the performance optimization of DAB converters, computational time becomes a critical factor, as multiple mathematical expressions must be evaluated a significant number of times to evaluate the converter performance for different operation points and modulation parameter values. In that sense, the expression of the inductor current is crucial, as its RMS value determines the conduction losses of the converter and the instantaneous value determines the power-semiconductor switching losses and the inductor magnetic-field peak value. Therefore, minimizing the computational time required to obtain these magnitudes is essential for developing a faster and more effective optimization tool.

A comparative analysis is conducted on the computational time required to obtain the instantaneous current and its RMS value, using both the compact analytical expressions and the Fourier analysis up to the 63rd harmonic. In performance studies using Fourier analysis, the number of harmonics determines the trade-off between calculation precision and computational time. In the present study, the maximum harmonic index has been selected such that the maximum error in the computation of the instantaneous current is less than 0.01 p.u.

The expressions for the instantaneous current from the proposed compact expressions (Equation (23)) and from the Fourier analysis (Equation (32)) are executed using MATLAB for 100 equally distributed values of θ in the range $[0, 2\pi]$. The current at each instant is computed 1000 times, resulting in a total of 100,000 executions. The expressions for the RMS current from the compact expressions (Equation (26)) and from the Fourier analysis (Equation (33)) are executed for 100 randomly generated operation points, defined by the values of the modulation angles. The RMS current for each operation point is computed 1000 times, also resulting in 100,000 executions. The computational time for each execution is measured, and the median computational time required for both currents and methods is obtained.

Table 5 shows the results of this analysis for 3, 4, 5, and 6 levels at side b of the converter. The results show a substantial reduction in computational time when using the compact analytical expression. The analysis reveals that, on average, employing the compact analytical expression allows to reduce by 34.6 times the computational time to obtain the instantaneous value for the inductor current. Furthermore, the computation of the RMS value is, on average, 2.9 times faster when using the compact analytical expression. The results obtained in the comparative computational time analysis then support the advantages of the proposed analytical approach.

Table 5. Median time to compute the instantaneous and RMS current using the proposed compact expressions and the Fourier approximation for $N = \{3, 4, 5, 6\}$.

	$N = 3$	$N = 4$	$N = 5$	$N = 6$
$t_{\text{iL,Fourier}}[\mu s]$	14.9	15.8	16.9	21.6
$t_{\text{iL,Comp}}[\mu s]$	0.5	0.5	0.5	0.5
$t_{\text{iLRMS,Fourier}}[\mu s]$	14.0	14.7	15.6	20.4
$t_{\text{iLRMS,Comp}}[\mu s]$	4.2	5.0	6.0	7.8

5. Discussion

The compact analytical expression for inductor current in ML DAB converters proposed in this paper significantly simplifies performance analysis. By using binary indicator functions, the piecewise nature of the current expression is generalized, allowing for efficient calculation of both instantaneous and RMS values for any arbitrary value of the modulation parameters and any given number of converter voltage levels. This generalization makes the performance analysis versatile and reduces the complexity associated with conventional methods.

The validation results, which agree with results from Fourier analysis, confirm the accuracy of the proposed method across different operating points. Furthermore, as shown in [5,15,18], the DAB inductor current waveforms obtained from an ideal lossless model and from experimental tests are very similar, and thus, the proposed method provides a fair trade-off between simplicity in the expressions and reproducibility of the real current and voltage waveforms. Moreover, the proposed method significantly reduces the computational time required to determine the inductor current in ML converters compared to the Fourier approximation.

These findings align with previous efforts in the field aimed at optimizing multilevel DAB converter topologies to enhance efficiency and reduce power losses, as seen in [5–7]. The method paves the way for optimization software tools that allow exploring multiple DAB converter structures and modulation strategies, without requiring ad hoc current expressions for each current mode. Applications like electric vehicles and renewable energy systems might benefit greatly from these tools.

Further work could explore applying this approach to DAB converter configurations with any arbitrary number of levels per side [22] and featuring other modulation techniques [23]. Furthermore, future work includes deriving generalized expressions for the soft-switching-region boundaries in different ML DAB converter topologies and modulation techniques [24,25]. Finally, the same approach can be extended to other converters with piecewise-defined inductor currents, such as the buck, boost, flyback, and resonant dc-dc converters.

Supplementary Materials: The following supporting information can be downloaded at: https://www.mdpi.com/article/10.3390/electronics13224476/s1, MATLAB m-file S1: MATLAB script intended for user execution to obtain the instantaneous inductor current and its RMS value in a ML DAB converter using the proposed mathematical method; MATLAB m-file S2: MATLAB function called by the S1 script to compute and return the instantaneous inductor current; MATLAB m-file S3: MATLAB function called by the S1 script to compute and return the inductor current RMS value.

Author Contributions: Conceptualization, methodology, investigation, validation: E.B.-P., O.E.-M., and A.F.-M.; software: E.B.-P.; formal analysis: E.B.-P.; resources: A.F.-M. and L.T.; writing—original draft preparation and review and editing: E.B.-P., O.E.-M., A.F.-M., and L.T.; supervision: O.E.-M. and A.F.-M.; project administration and funding acquisition: A.F.-M. and L.T. All authors have read and agreed to the published version of the manuscript.

Funding: This work was funded by the European Union's Horizon Europe research and innovation program under grant agreement No. 101056781. Views and opinions expressed are, however, those of the author(s) only and do not necessarily reflect those of the European Union or CINEA. Neither the European Union nor the granting authority can be held responsible for them.

Data Availability Statement: The original contributions presented in this study are included in the article and supplementary material. Further inquiries can be directed to the corresponding author(s).

Conflicts of Interest: The authors declare no conflict of interest.

References

1. Hou, N.; Li, Y.W. Overview and Comparison of Modulation and Control Strategies for a Nonresonant Single-Phase Dual-Active-Bridge DC–DC Converter. *IEEE Trans. Power Electron.* **2020**, *35*, 3148–3172. [CrossRef]
2. Bughneda, A.; Salem, M.; Richelli, A.; Ishak, D.; Alatai, S. Review of Multilevel Inverters for PV Energy System Applications. *Energies* **2021**, *14*, 1585. [CrossRef]
3. Kouro, S.; Malinowski, M.; Gopakumar, K.; Pou, J.; Franquelo, L.G.; Wu, B.; Rodriguez, J.; Pérez, M.A.; Leon, J.I. Recent Advances and Industrial Applications of Multilevel Converters. *IEEE Trans. Ind. Electron.* **2010**, *57*, 2553–2580. [CrossRef]
4. Busquets-Monge, S. Neutral-Point-Clamped DC–AC Power Converters. In *Wiley Encyclopedia of Electrical and Electronics Engineering*; John Wiley & Sons, Ltd.: Hoboken, NJ, USA, 2018; pp. 1–20.
5. Filba-Martinez, A.; Busquets-Monge, S.; Nicolas-Apruzzese, J.; Bordonau, J. Operating principle and performance optimization of a three-level NPC dual-active-bridge DC–DC converter. *IEEE Trans. Ind. Electron.* **2015**, *63*, 678–690. [CrossRef]
6. Liu, P.; Chen, C.; Duan, S. An Optimized Modulation Strategy for the Three-Level DAB Converter With Five Control Degrees of Freedom. *IEEE Trans. Ind. Electron.* **2020**, *67*, 254–264. [CrossRef]
7. Song, C.; Sangwongwanich, A.; Yang, Y.; Blaabjerg, F. Optimal Control of Multilevel DAB Converters for Soft-Switching and Minimum Current Stress. *IEEE Trans. Power Electron.* **2024**, *39*, 5707–5720. [CrossRef]
8. Niu, J.; Yang, X.; Su, D.; Zhao, K.; Li, S. Study of Transient Control Performance of Cascaded NPC-DAB for Power Supply System of Data Center. In Proceedings of the 2023 11th International Conference on Power Electronics and ECCE Asia (ICPE 2023—ECCE Asia), Jeju Island, Republic of Korea, 22–25 May 2023; pp. 400–405.
9. Yun, H.J.; Jeong, D.K.; Kim, H.S.; Kim, M.; Baek, J.W.; Kim, J.Y.; Kim, H.J. Implementation of a Single-Phase SST for the Interface between a 13.2 kV MVAC Network and a 750 V Bipolar DC Distribution. *Electronics* **2018**, *7*, 62. [CrossRef]
10. Shi, Y.; Li, R.; Li, H. Modular multilevel dual active bridge DC-DC converter with ZVS and fast DC fault recovery for battery energy storage systems. In Proceedings of the 2016 IEEE Applied Power Electronics Conference and Exposition (APEC), Long Beach, CA, USA, 20–24 March 2016; pp. 1675–1681.
11. Tian, J.; Zhuo, C.; Wang, F.; Deng, H. An RMS Current Minimization Method for Three-Level ANPC-DAB-Based Distributed Energy Storage System With Full Operation ZVS. *IEEE J. Emerg. Sel. Top. Power Electron.* **2024**, *12*, 2388–2405. [CrossRef]
12. Chaurasiya, S.; Singh, B. A bidirectional fast EV charger for wide voltage range using three-level DAB based on current and voltage stress optimization. *IEEE Trans. Transp. Electrif.* **2022**, *9*, 1330–1340. [CrossRef]
13. Xuan, Y.; Yang, X.; Chen, W.; Liu, T.; Hao, X. A Three-Level Dual-Active-Bridge Converter With Blocking Capacitors for Bidirectional Electric Vehicle Charger. *IEEE Access* **2019**, *7*, 173838–173847. [CrossRef]
14. Lee, J.Y.; Cho, Y.P.; Jung, J.H. Single-stage voltage balancer with high-frequency isolation for bipolar LVDC distribution system. *IEEE Trans. Ind. Electron.* **2019**, *67*, 3596–3606. [CrossRef]
15. Kolahian, P.; Tarzamni, H.; Nikafrooz, A.; Hamzeh, M. Multi-port DC–DC converter for bipolar medium voltage DC micro-grid applications. *IET Power Electron.* **2019**, *12*, 1841–1849. [CrossRef]
16. Kong, X.; Zhang, J.; Zhou, J.; Zang, J.; Wang, J.; Shi, G.; Cai, X. Power and Voltage Control Based on DC Offset Injection for Bipolar Low-Voltage DC Distribution System. *J. Mod. Power Syst. Clean Energy* **2022**, *11*, 1529–1539. [CrossRef]
17. Kong, X.; Li, L.; Zhang, J.; Wang, H.; Zhou, J.; Shi, G.; Cai, X. Operation and Control of DC Solid State Transformer With Bipolar LVDC Ports. In Proceedings of the 2021 IEEE 12th Energy Conversion Congress and Exposition—Asia (ECCE-Asia), Singapore, 24–27 May 2021; pp. 402–407.

18. Krismer, F.; Kolar, J.W. Closed Form Solution for Minimum Conduction Loss Modulation of DAB Converters. *IEEE Trans. Power Electron.* **2012**, *27*, 174–188. [CrossRef]
19. Capó-Lliteras, M.; Oggier, G.G.; Bullich-Massagué, E.; Heredero-Peris, D.; Montesinos-Miracle, D. Analytical and Normalized Equations to Implement the Optimized Triple Phase-Shift Modulation Strategy for DAB Converters. *IEEE J. Emerg. Sel. Top. Power Electron.* **2023**, *11*, 3535–3546. [CrossRef]
20. Higa, H.; Itoh, J.i. Derivation of operation mode for flying capacitor topology applied to three-level DAB converter. In Proceedings of the Future Energy Electronics Conference (IFEEC), 2015 IEEE 2nd International, Taipei, Taiwan, 1–4 November 2015; pp. 1–6.
21. Kenzelmann, S.; Rufer, A.; Dujic, D.; Canales, F.; de Novaes, Y.R. Isolated DC/DC Structure Based on Modular Multilevel Converter. *IEEE Trans. Power Electron.* **2015**, *30*, 89–98. [CrossRef]
22. Filba-Martinez, A.; Busquets-Monge, S.; Bordonau, J. Modulation and Capacitor Voltage Balancing Control of Multilevel NPC Dual Active Bridge DC–DC Converters. *IEEE Trans. Ind. Electron.* **2020**, *67*, 2499–2510. [CrossRef]
23. Lee, J.Y.; Choi, H.J.; Jung, J.H. Three level NPC dual active bridge capacitor voltage balancing switching modulation. In Proceedings of the 2017 IEEE International Telecommunications Energy Conference (INTELEC), Gold Coast, Australia, 22–26 October 2017; pp. 438–443.
24. Liu, J.; Chen, W.; Ma, X.; Zhang, R.; Yan, R. A zero voltage switching range optimization strategy for NPC Dual-Active-Bridge Converter. In Proceedings of the 2020 4th International Conference on HVDC (HVDC), Xi'an, China, 6–9 November 2020; pp. 966–970.
25. Patil, N.S.; Shukla, A. Peak Current Optimization of Hybrid NPC-DAB Converter Ensuring Soft Switching of All the Switches. In Proceedings of the 2023 IEEE Energy Conversion Congress and Exposition (ECCE), Nashville, TN, USA, 29 October–2 November 2023; pp. 3380–3385.

Disclaimer/Publisher's Note: The statements, opinions and data contained in all publications are solely those of the individual author(s) and contributor(s) and not of MDPI and/or the editor(s). MDPI and/or the editor(s) disclaim responsibility for any injury to people or property resulting from any ideas, methods, instructions or products referred to in the content.